ELSEVIER

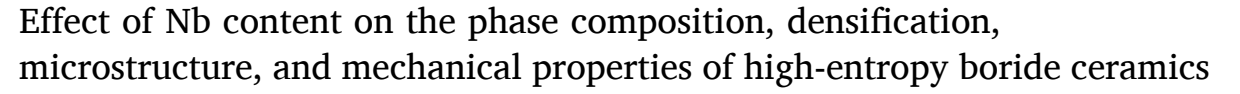
Contents lists available at ScienceDirect

Journal of the European Ceramic Society

journal homepage: www.elsevier.com/locate/jeurceramsoc

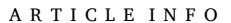


Original Article



Lun Feng ^{a, *}, William G. Fahrenholtz ^a, Gregory E. Hilmas ^a, Frédéric Monteverde ^b

- ^a Department of Materials Science and Engineering, Missouri University of Science and Technology, Rolla, MO, 65049, USA
- ^b National Research Council of Italy, Institute of Science and Technology for Ceramic, Faenza, RA, 48018, Italy



Keywords:
High-entropy borides
Nb segregation
Densification
Microstructure
Mechanical properties

ABSTRACT

Dense high-entropy (Hf,Zr,Ti,Ta,Nb)B $_2$ ceramics with Nb contents ranging from 0 to 20 at% were produced by a two-step spark plasma sintering process. X-ray diffraction indicated that a single-phase with hexagonal structure was detected in the composition without Nb. In contrast, two phases with the same hexagonal structure, but slightly different lattice parameters were present in compositions containing Nb. The addition of Nb resulted in the presence of a Nb-rich second phase and the amount of the second phase increased as the Nb content increased. The relative densities were all >99.5 %, but decreased from ~ 100 % to ~ 99.5 % as the Nb content increased from 0 to 20 at%. The average grain size decreased from 13.9 ± 5.5 µm for the composition without Nb additions to 5.2 ± 2.0 µm for the composition containing 20 at% Nb. The reduction of grain size with increasing Nb content was due to the suppression of grain growth by the Nb-rich second phase. The addition of Nb increased Young's modulus and Vickers hardness, but decreased shear modulus. While some Nb dissolved into the main phase, a Nb-rich second phase was formed in all Nb-containing compositions.

1. Introduction

Recently, high-entropy boride (HEB) ceramics, a new class of ultrahigh temperature ceramics (UHTCs), have attracted considerable interest due to their potential for improved mechanical properties and thermal stability compared to individual transition metal diboride ceramics [1–6]. Many studies have been performed to investigate the synthesis and properties of HEB ceramics due to their potential for use in extreme environments [1,4–17].

Single-phase HEB ceramics with the AlB₂-type structure can be formed by solid solutions of four or more transition metal borides [4–6, 18]. These ceramics are strongly refractory and typically exhibit poor sinterability due to the strong bonding and low self-diffusion coefficients of the individual transition metal diborides [1,3,19]. Gild et al. [4] produced several different HEB ceramics by spark plasma sintering (SPS) commercial diboride powders at 2000 °C under a uniaxial pressure of 30 MPa. Among them, (Hf,Zr,Ta,Nb,Ti)B₂, (Hf,Zr,Ta,Mo,Ti)B₂, (Hf,Zr,Ta,Nb,Ti)B₂, (Mo,Zr,Ta,Nb,Ti)B₂ and (Hf,Zr,Ta,Cr,Ti)B₂ ceramics appeared to be nominally single-phase with relative densities of ~92 %, and Vickers hardness values, at a load of 200 kgf/mm², in the range of ~17 to ~24 GPa. However, a residual (Ti,W)B₂

phase was detected in (Hf,Zr,W,Mo,Ti)B $_2$ ceramics, which indicated that solid solution was not complete. The presence of residual oxide impurities was also noted in those ceramics. Oxides were presumed to inhibit densification and result in better relative densities. The oxide impurities originated from surface oxides present on the initial commercial diboride powders, and oxygen content was further increased by high-energy ball milling (HEBM) of the starting powders. Similarly, Tallarita et al. [13,14] produced (Hf,Mo,Ta,Nb,Ti)B $_2$ ceramics by SPS at 1950 °C under a uniaxial pressure of 30 MPa using powder mixtures synthesized by self-propagating high-temperature synthesis (SHS). The resulting ceramics had relative densities of 92.5 % due to the presence of residual oxides and unreacted B in HEB powder mixtures, both of which inhibit densification.

To improve the purity and sinterability of HEB ceramics, several groups have synthesized HEB powders with finer particle size. Zhang et al. [15,16] produced (Hf,Zr,Ta,Nb,Ti)B₂, (Hf,Zr,Ta,Cr,Ti)B₂, (Hf,Mo,Zr,Nb,Ti)B₂, and (Hf,Mo,Ta,Nb,Ti)B₂ ceramics from boride powder mixtures synthesized by boro/carbothermal reduction (BCTR) of transition metal oxides. The resulting HEB ceramics had higher relative densities, in the range of 95%–99%, compared to HEB ceramics produced from pre-reacted commercial diboride powders [4]. The increase

E-mail address: allen13521@gmail.com (L. Feng).

^{*} Corresponding author.

Table 1Composition designations and metal contents of HEB ceramics with different Nb contents. Full boron stoichiometry, i.e., TMB₂, was assumed for all compositions.

Abbreviations	Hf	Zr	Ti	Ta	Nb
HEBON	25.0	25.0	25.0	25.0	0
HEB5N	23.75	23.75	23.75	23.75	5.0
HEB20N	20.0	20.0	20.0	20.0	20.0

in relative density was attributed to particle sizes in the range of 0.2 µm to 0.5 μm in the synthesized powders. However, up to ~7.2 wt% of residual oxide impurities was observed in final ceramics due to the residual oxide impurities in synthesized powder mixtures. The resulting HEB ceramics had an average grain size of less than 2 μm, Vickers hardness values ranging from ${\sim}22$ GPa to ${\sim}28$ GPa, and fracture toughness values approaching 4 MPa $m^{1/2}$. Subsequently, fully dense (Hf,Zr,Ti,Ta,Nb)B₂ ceramics with lower oxygen (0.004 wt%) contents and low residual carbon (0.018 wt%) contents were produced by a two-step SPS process using powder mixtures synthesized by BCTR of oxides incorporating excess B₄C. [15] Higher relative densities of the final HEB ceramics were achieved compared to the results from other studies [4,12–16] due to finer particle sizes ($\sim\!0.3\,\mu\text{m})$ of the synthesized powder, and lower oxygen (0.404 wt%) and carbon (0.034 wt%) contents [5,9]. Vickers hardness (HV_{0,2}) of the resulting (Hf,Zr,Ti,Ta,Nb)B₂ ceramics were higher than previous studies, in the range of ~24 GPa to ~26 GPa, due to the higher relative densities, finer grain sizes, and lower oxygen contents [4,16].

The incorporation of atoms with different atomic sizes into a single crystal lattice can change the local chemical bonding environment, which would affect the properties of the resulting ceramics. Previous studies reported that HEB ceramics exhibited higher hardness than expected based on the hardness values of the individual diboride ceramics, which was attributed to disorder associated with the presence of multiple transition metals and solid solution hardening [20,21]. Previous studies of HEB ceramics focused only on the compositions with equal metal atom ratios. Some studies have reported an inhomogeneous distribution of Nb in HEB ceramics [4,6,12,15–17]. Nb-rich regions were observed in (Hf_{0.2},Zr_{0.2},Ti_{0.2},Ta_{0.2},Nb_{0.2})B₂ ceramics produced by both SPS at \sim 2050 °C with dwell times ranging from 5 min to 10 min [4,12, 16,17] and hot pressing (HP) at 1927 °C for 14 min [6]. Nb segregation could be due to the slow diffusion of Nb during solid solution formation for HEB ceramics at low sintering temperature and/or short diffusion times. However, effects of Nb on the properties of HEB ceramics has not been further studied.

The purpose of this study was to investigate the effect of Nb content on the phase composition, densification, microstructure, mechanical properties of (Hf,Zr,Ti,Ta,Nb)B₂ ceramics.

2. Experimental procedures

Hafnium oxide (HfO₂, 99 %, -325 mesh; Alfa Aesar, Tewksbury, MA), tantalum oxide (Ta₂O₅, 99.8 %, 1–5 µm; Atlantic Equipment Engineers, Upper Saddle River, NJ), titanium oxide (TiO2, 99.9 %, 32 nm APS; Alfa Aesar), zirconium oxide (ZrO₂, 99 %, 5 μm; Sigma-Aldrich, St. Louis, MO), niobium oxide (Nb₂O₅, 99.5 %, -100 mesh; Alfa Aesar), boron carbide (B₄C, purity 96.8 %, $0.6\sim1.2~\mu m$, H.C. Starck, Newton, MA) and carbon black (C, BP1100, Cabot, Alpharetta, GA) were used as the starting materials. Three different compositions were selected to produce HEB ceramics with different Nb contents. (Table 1) Oxides were batched with 11 wt% excess B₄C and the stoichiometric amount of C to produce HEB ceramics, as described in detail in a previous paper from our group [5]. HEB powder mixtures were synthesized by BCTR at 1650 °C for 3 h under mild vacuum (~3 Pa). Subsequently, HEB ceramics were produced from the same amount of synthesized powders by two-step SPS with a peak temperature of 2100 $^{\circ}\text{C}$ under mild vacuum (~2 Pa). An isothermal hold at 1650 °C for 5 min under a uniaxial

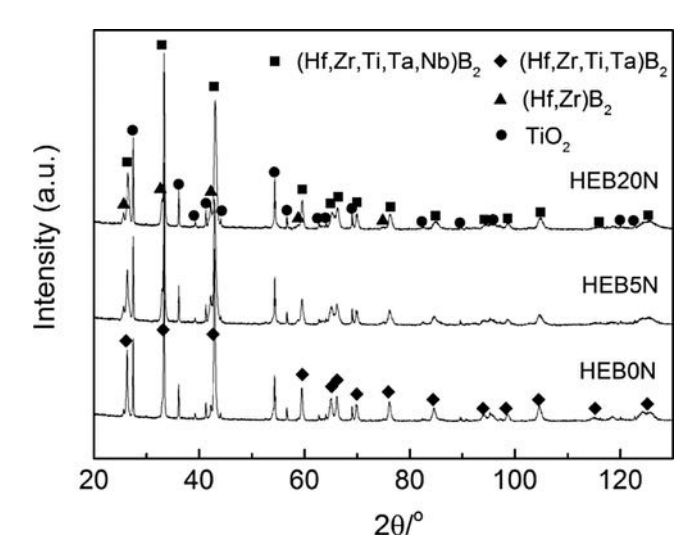


Fig. 1. XRD patterns of HEB0N, HEB5N and HEB20N synthesized at 1650 $^{\circ}\text{C}$ by BCTR.

pressure of 15 MPa was applied to promote removal of residual oxide impurities. The shrinkage curves were recorded and then corrected by adjusting total ram displacement to compensate for the thermal expansion of the graphite die, which was done by recording dimensional changes for an empty graphite die heated using the same sintering profile as the powders.

Phase compositions of HEB powder mixtures were determined by xray diffraction analysis (XRD, PANalytical X-Pert Pro, Malvern Panalytical Ltd., Royston, United Kingdom). XRD patterns were obtained by scanning from 10° to 135° 2-theta with Ni-filtered Cu-K α radiation, a step size of 0.026°, and an effective counting time of 42.84 s for each step. For some analyses, TiO2 was added as an internal standard for calibration of peak positions. The morphologies and particle sizes of powder mixtures were examined using field-emission scanning electron microscopy (FESEM, S4700, Hitachi, Tokyo, Japan). A computer-based image analysis program (ImageJ, National Institutes of Health, Bethesda, MD) was used to estimate the average particle sizes. At least 300 grains were analyzed for each reported average. Sintered disks that were 20 mm in diameter were ground on both sides to remove the graphite foil and any reaction layers. Bulk densities were measured by Archimedes' method using distilled water as the immersing medium. Phase compositions of sintered specimens were determined from XRD patterns which were obtained using the same scanning parameters as for the powder. Rietveld refinement was performed using RIQAS software (MDI) to estimate the lattice parameters. Theoretical densities were calculated from the measured lattice parameters and the nominal ratios of transition metals from the batched precursors. Microstructures, grain sizes, chemical composition, and distributions of metals were examined using SEM (FEI Helios NanoLab 600, FEI) with energy dispersive spectroscopy (EDS; Oxford EDS, Oxford Instruments). Specimens surface were polished to a 0.25 µm finish using successively finer diamond suspensions. Grain sizes were estimated by analyzing SEM images using computerized image analysis of at least 250 grains per specimen.

Young's modulus and shear modulus were measured using a dynamic elastic properties analyzer using an ultrasonic method (DEPA, Jagdish Electronics, Karnataka, India). Microhardness was measured by Vickers indentation following ASTM C1327 (Model Duramin 5, Struers Inc., Cleveland, OH), under indentation loads of 2.0 N, 4.9 N, and 9.8 N for a dwell time of 15 s. Reported values are the average of 10 measurements.

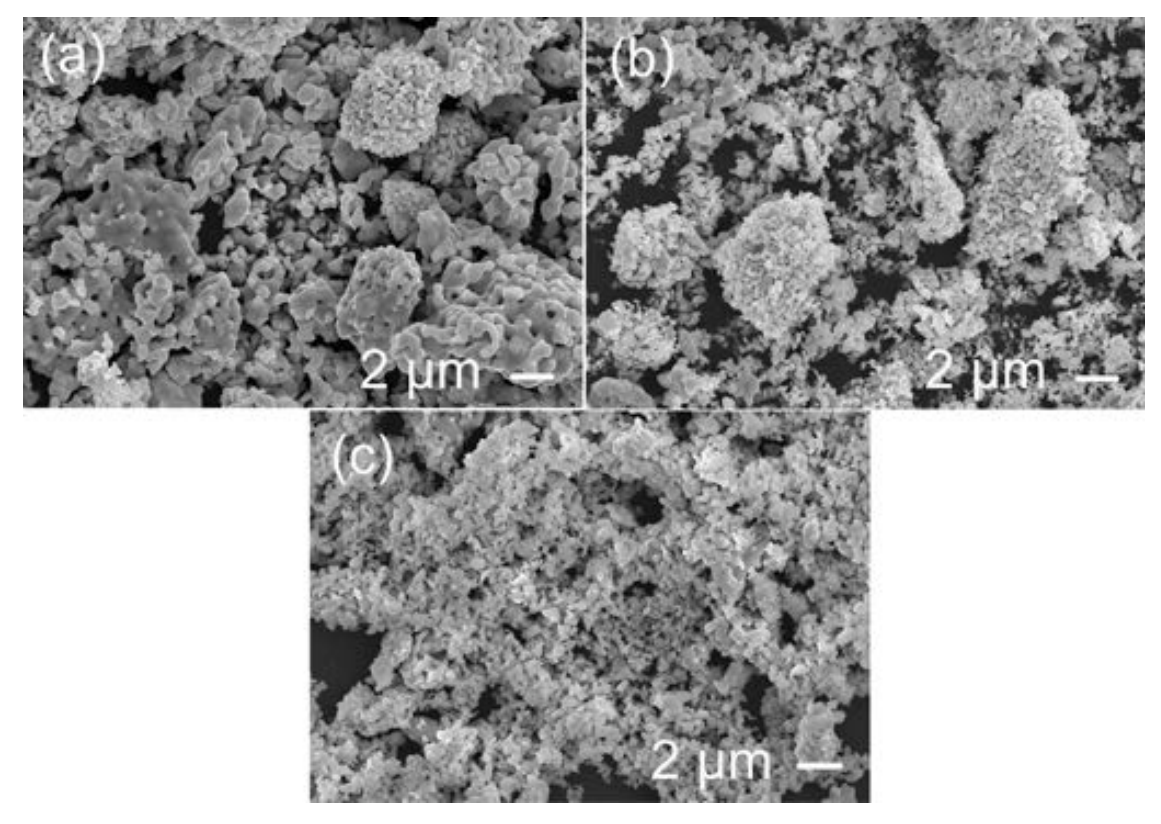


Fig. 2. Morphologies of (a) HEBON, (b) HEB5N and (c) HEB20N synthesized at 1650 °C by BCTR.

3. Results and discussion

3.1. Characterizations of synthesized HEB powder mixtures

Fig. 1 shows XRD patterns of the HEB powders with different Nb contents synthesized by BCTR at 1650 °C. Based on our previous studies [5,9], XRD patterns indicated that at least two distinct boride phases with the same hexagonal structure, but different lattice parameters, were present in all powder mixtures. The phases present in HEBON were nominally identified as (Hf,Zr,Ti,Ta)B2 and (Hf,Zr)B2, while the phases present in HEB5N and HEB20N were nominally identified as (Hf,Zr,Ti, Ta,Nb)B2 and (Hf,Zr)B2. Analysis of powder mixtures was performed assuming the presence of only two phases, but the possibility exists for the presence of additional phases, which is the subject of a planned future study. For the present analysis, no residual oxides were detected in any of the synthesized powders. Note that TiO₂ was detected because it was added as an internal standard to quantify peak positions. These results indicated that the BCTR reactions went to completion at 1650 $^{\circ}\text{C}$ when 11 wt% excess B₄C was added, even though solid solution formation was not complete.

Fig. 2 shows the morphologies of HEB0N, HEB5N and HEB20N synthesized at 1650 °C. Agglomerates were observed in all powder mixtures, which likely originated from agglomerates formed by cold welding during HEBM of the starting powders [9,22]. Strong agglomerates containing particles of different sizes were observed in HEB0N. Some agglomerates were composed of fine particles ranging from $\sim\!0.3~\mu m$ to $\sim\!0.5~\mu m$, while some agglomerates were composed of larger particles ranging from $\sim\!0.7~\mu m$ to $\sim\!1.0~\mu m$. Neck formation was observed between large particles, which indicated that significant grain growth occurred during BCTR. The average particle size of HEB0N was estimated to be $0.6\pm0.3~\mu m$. In contrast, HEB5N and HEB20N had more homogenous and finer particle sizes, which were both estimated to be $0.3\pm0.2~\mu m$. The addition of Nb resulted in finer particle size of HEB powder mixtures, presumably due to enhancement of the solid solution

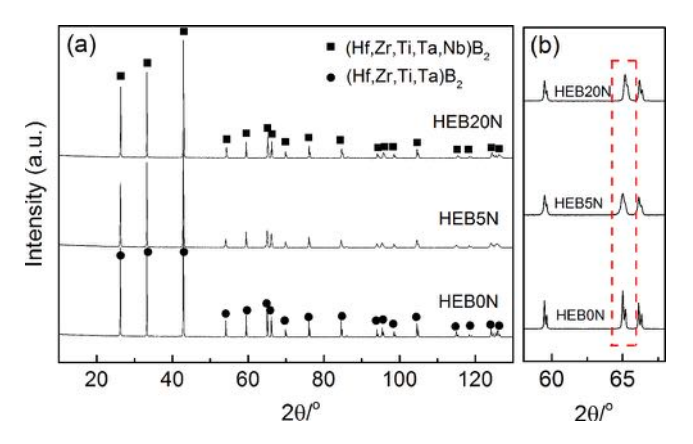


Fig. 3. XRD patterns of HEB0N, HEB5N and HEB20N produced at 2100 $^{\circ}\text{C}$ by two-step SPS.

effect caused by introducing additional components.

3.2. Phase composition of HEB ceramics

Fig. 3 shows the effect of Nb content on the phase composition of HEB ceramics after densification at 2100 $^{\circ}$ C. Based on the XRD results, no oxides were detected in any specimens, which was attributed to the low oxygen content of HEB powder mixtures and the application of an isothermal hold at 1650 $^{\circ}$ C during SPS [5]. The pattern for HEB0N was consistent with a single HEB phase, nominally (Hf,Zr,Ti,Ta)B₂. Based on evidence from SEM-EDS discussed below, phase separation was present the sintered specimens containing Nb. The addition of Nb did not lead to any apparent changes in the peaks at lower angles (i.e., below 60 $^{\circ}$). However, when 5 at% Nb was added, changes were observed in the peaks present at around 65 $^{\circ}$ or higher (Fig. 3(b)). For HEB0N, a doublet was present at about 65 $^{\circ}$. The peak splitting was not present at lower

Table 2Lattice parameters (a, c, and c/a) of HEB ceramics compared to values of individual transition metal borides.

Abbreviations	Main phase	Main phase			Secondary phase		
	a (nm)	c (nm)	c/a	a (nm)	c (nm)	c/a	Refs.
HEB0N	0.31056(4)	0.33881(5)	1.0910	_	_	_	
HEB5N	0.31059(4)	0.33901(5)	1.0915	0.31055(4)	0.33862(5)	1.0904	Present work
HEB20N	0.31053(4)	0.33779(5)	1.0878	0.31053(4)	0.33738(5)	1.0865	
HfB_2	0.3141	0.3470	1.1047	_	_	_	
ZrB_2	0.3169	0.3530	1.1139	_	_	_	
TiB ₂	0.3028	0.3228	1.0661	_	_	_	[3,23,24]
TaB ₂	0.3097	0.3225	1.0413	_	_	_	
NbB_2	0.3110	0.3270	1.0514	_	_	_	

Table 3Sintering conditions, theoretical densities, relative densities, mechanical properties, and average grain sizes of HEB ceramics with different Nb contents.

Abbreviations	Parameters (°C/MPa/min)	Theoretical density (g/cm³)	Relative density (%)	Young's modulus (GPa)	Shear modulus (GPa)	Vickers hardness (Hv0.2, GPa)	Average grain siz (µm)	Ref.
HEBON (Hf _{0.25} Zr _{0.25} Ti _{0.25} Ta _{0.25})B ₂	SPS/2100/50/ 10	8.58	100	534 ± 7	235 ± 3	23.7 ± 0.3	13.9 ± 5.5	
HEB5N ($Hf_{0.2375}Zr_{0.2375}Ti_{0.2375}Ta_{0.2375}Nb_{0.2375}$) B_2	SPS/2100/50/ 10	8.48	99.8	555 ± 8	231 ± 3	23.1 ± 0.9	5.6 ± 2.1	Present study
HEB20N ($Hf_{0.2}Zr_{0.2}Ti_{0.2}Ta_{0.2}Nb_{0.2}$) B_2	SPS/2100/50/ 10	8.24	99.5	544 ± 8	221 ± 3	25.3 ± 0.6	5.2 ± 2.0	
$(Hf_{0.2}Zr_{0.2}Ti_{0.2}Ta_{0.2}Nb_{0.2})B_2 \\$	SPS/2000/30/ 5	8.34	92.4	-	_	17.5 ± 1.2	_	[4]
$(Hf_{0.2}Zr_{0.2}Ti_{0.2}Ta_{0.2}Nb_{0.2})B_2 \\$	HP/1927/50/ 12	8.27	98.7	-	-	22.7 ± 1.9	0.3~1	[6]
$(Hf_{0.2}Zr_{0.2}Ti_{0.2}Ta_{0.2}Nb_{0.2})B_2$	SPS/2000/50/ 5	8.24	94.4	500	-	25.6 ± 0.8	6.67 ± 1.2	[12]
$(Hf_{0.2}Zr_{0.2}Ti_{0.2}Ta_{0.2}Nb_{0.2})B_2 \\$	SPS/2000/30/ 10	8.27	96.3	-	_	21.7 ± 1.1	1.6	[16]

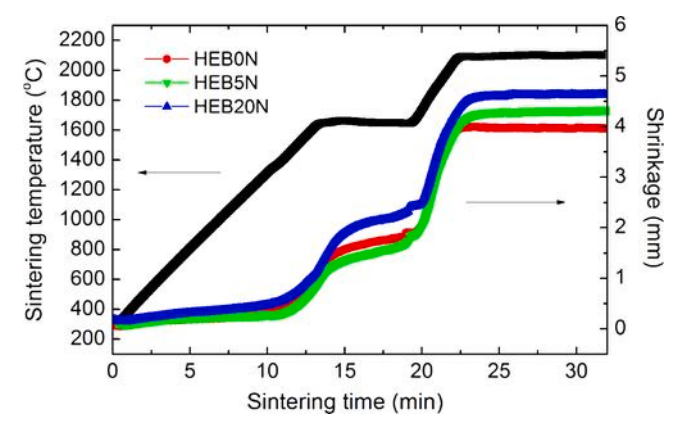


Fig. 4. Shrinkage curves as a function of sintering time for HEB0N, HEB5N and HEB20N during two-step SPS at 2100 $^{\circ}\text{C}.$

angles. The splitting of the higher angle peaks in HEB0N is consistent with the presence of both Cu-K α_1 ($\lambda=1.540562$ Å) and Cu-K α_2 ($\lambda=1.544390$ Å) radiation in the incident x-ray beam, which led to the formation of peaks at 65.00° and 65.20° for the same (111) plane in the HEB structure with a d-spacing of ~ 1.429 Å. When Nb was added, the doublet merged into what appeared to be a single, broader peak for the HEB5N and HEB20N patterns. The apparent broadening could be due to lattice strain or due to the emergence of additional peaks with similar lattice parameters (Table 2). Overall, the XRD results can be interpreted to support the presence of two (or possibly more) HEB phases in the dense ceramics. More precise quantitative analysis on these HEB phases will be one object of a further study.

3.3. Densification behavior

The relative density of HEB0N was 100 %, while the relative density decreased to 99.7 % for HEB5N and 99.4 % for HEB20N. (Table 3) Previous studies reported that solid solution formation likely promoted the densification of ceramics [25,26]. However, the results obtained in the present study showed that the densification of HEB ceramics was inhibited by the addition of Nb, which could be due to changes in densification kinetics cause by Nb dissolved in the HEB phase [27,28] and /or the presence of the second HEB phase.

Fig. 4 shows the shrinkage curves as a function of sintering time during the two-step SPS process. All of the specimens had similar shrinkage curves. Below about 1400 °C, a small amount of shrinkage was observed, which was attributed to particle re-arrangement under the light load that was applied during heating of the SPS. Significant shrinkage occurred above about 1400 °C and throughout the entire isothermal hold at 1650 °C, which indicated that densification was not complete with the combination of low sintering temperature (<1650 °C) and low uniaxial pressure (15 MPa). After the isothermal hold at 1650 °C, a sharp increase in shrinkage was observed due to the application of a higher uniaxial pressure of 50 MPa for the second stage of the densification cycle. Subsequently, distinct shrinkage occurred until the final densification temperature of 2100 °C was reached. Finally, shrinkage decreased and stopped during the final isothermal hold as closed pores were eliminated. For HEBON, a horizontal shrinkage curve was observed during the final isothermal hold, which indicated shrinkage stopped before the final isothermal hold temperature was reached. In contrast, slightly higher slopes were observed for HEB5N and HEB20N, compared to that of HEBON, which indicated that shrinkage continued during the final isothermal hold. The results were consistent with the higher measured relative density of HEBON compared to HEB5N and HEB20N. (Table 3) These results indicated that the addition of Nb inhibited the

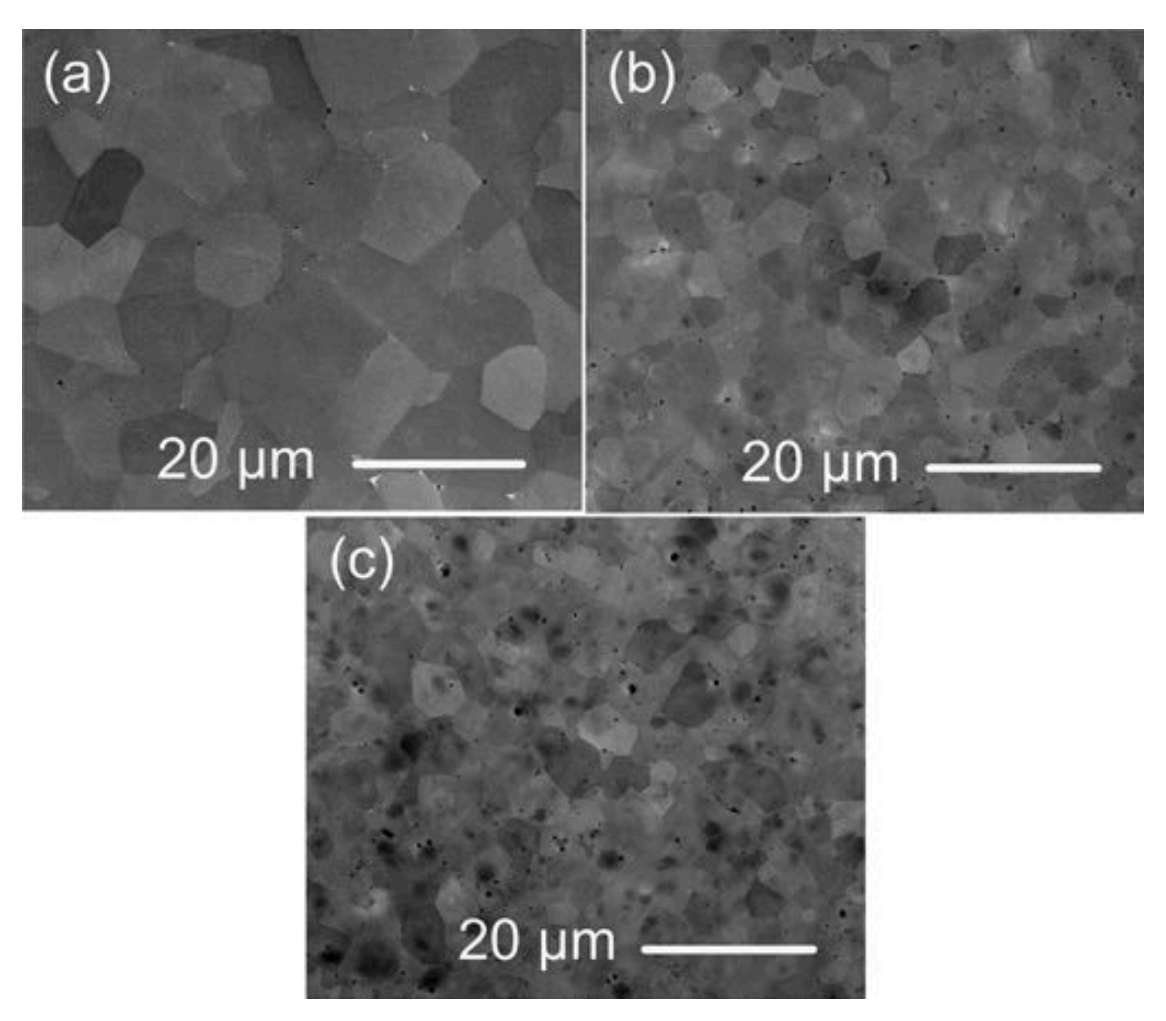


Fig. 5. SEM images of (a) HEBON, (b) HEB5N and (c) HEB20N.

densification of ceramics in the (Hf,Zr,Ti,Ta)B2 system.

3.4. Microstructure

Fig. 5 shows the microstructures of HEBON, HEB5N and HEB20N after densification at 2100 °C. A fully dense microstructure was observed for HEBON, although trace amounts of oxides were observed as small inclusions at grain boundaries. In contrast, a small volume fraction of residual porosity was observed at grain boundaries for HEB5N and HEB20N. These results indicated that the amount of residual porosity increased as Nb content increased, which was consistent with the measured relative densities and observed densification behavior. The average grain sizes were 13.9 \pm 5.5 μm for HEBON, 5.6 \pm 2.1 μm for HEB5N, and 5.2 \pm 2.0 μm for HEB20N. (Table 3) The results indicated that the addition of Nb reduced grain sizes of HEB ceramics. The additional transition metal has also been shown to affect densification and grain growth of diboride ceramics, which could have also contributed to the suppression of grain growth in the HEB ceramics containing Nb [27, 28]. The grain size of ($Hf_{0.2}$, $Zr_{0.2}$, $Ti_{0.2}$, $Ta_{0.2}$, $Nb_{0.2}$) B_2 ceramics was 5.2 \pm 2.0 μm , which was smaller than 6.67 \pm 1.2 μm reported in a previous paper due to benefits of the two-step sintering process used in the present study [5]. However, grain size in the present study was larger than the values ranging from 0.3 μm to 1.6 μm in other studies [6,16], because the presence of residual impurities (i.e., oxides and B₄C) and porosity in those materials suppressed grain growth.

The distributions of metal elements were analyzed to characterize the second HEB phase that was observed. The corresponding EDS maps of HEBON, HEB5N and HEB20N are shown in Fig. 6. For HEBON, Hf, Zr, Ti and Ta were distributed uniformly in the scanned area, which was consistent with the single HEB phase detected by XRD. In contrast, for HEB5N and HEB20N, Nb-rich areas were also detected while Hf, Zr, Ti, and Ta were uniformly distributed. In addition, the number of Nb-rich areas in HEB20N was significantly higher than those in HEB5N. The results indicated that the addition of Nb to the HEB resulted in the Nb segregation, and higher Nb additions enhanced Nb segregation in HEB ceramics.

The metal elements were distributed uniformly in HEBON, which resulted in a uniform appearance of the grains in the microstructure. (Fig. 6(a)) However, darker areas were observed for HEB5N and for HEB20 N. (Fig. 6(b) and (c)) Such darker areas were Nb-rich compared to the surrounding areas shown by the corresponding SEM-EDS maps. Table 4 summarizes the SEM-EDS data for the areas labeled with numbers 1-10 shown in Fig. 6. For HEBON, areas 1-3 had almost equal metal atoms contents, with each corresponding to ~25 at%, indicating that Hf, Zr, Ti and Ta contents were consistent with the starting composition and that the metals were uniformly distributed on the scale of the microstructure (Table 1). For HEB5N, areas 4 and 7 exhibited normal contrast and had similar metal atom contents to the starting compositions, while areas 5 and 6 appeared darker and showed higher Nb contents (34.9 at% and 58.2 at%) than the starting amount (5 at%). Similarly, for HEB20N, areas 8 and 9 had darker contrast and had Nb contents of 55.8 at% and 59.1 at% that were much higher than the overall composition (20 at%). The results indicated that the dark areas in both HEB5N and HEB20N had similar Nb contents despite the difference in overall Nb content. As a result, the number of Nb-rich (dark) areas increased as the addition of Nb increased, indicating the size and

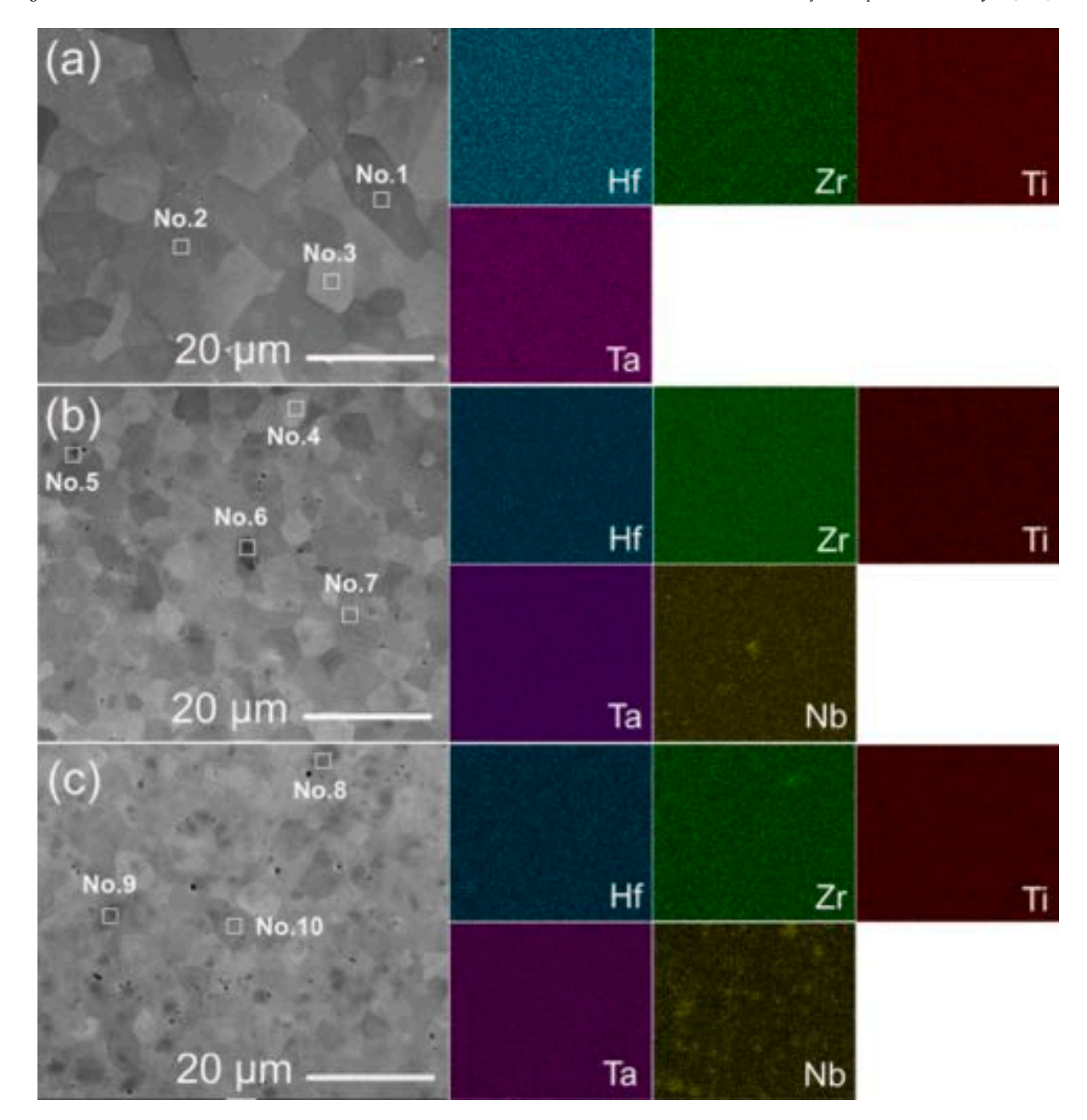


Fig. 6. Microstructures and corresponding EDS maps of (a) HEB0N, (b) HEB5N and (c) HEB20N (No. 1-10: EDS positions).

Table 4
EDS data for HEB ceramics shown in Fig. 6.

Abbreviations	Points	Element	Elements (at%)						
	Politis	Hf	Zr	Ti	Ta	Nb			
HEB0N	No.1	23.4	24.9	27.3	24.4	_			
	No.2	23.3	24.6	27.4	24.7	_			
	No.3	22.7	25.5	27.5	24.3	_			
HEB5N	No.4	23.9	23.9	23.5	25.0	3.7			
	No.5	15.3	16.1	18.7	15.0	34.9			
	No.6	10.1	11.4	12.3	8.1	58.2			
	No.7	20.9	23.4	25.6	25.7	4.4			
HEB20N	No.8	9.3	10.8	11.3	9.5	59.1			
	No.9	11.2	10.8	12.0	10.1	55.8			
	No.10	20.8	19.2	22.0	22.2	15.9			

amount of the Nb-rich phase increased. In order to maximize the representative size of the Nb-rich regions against the spatial resolution of the SEM-EDS technique, only the HEB20N material was used to quantitatively analyze the elemental distribution of various transition metals present inside the Nb-rich regions. A region with several Nb-rich features surrounded by the main (Ti,Ta,Hf,Zr,Nb)B₂ phase are shown in Fig. 7. Based on the SEM-EDS analysis, the main phase had approximately the same composition as the nominal starting HEB composition, while the second phase was Nb-rich. Quantitative EDS line scans (Fig. 8) revealed two interesting characteristics related to the Nb-rich phase: 1) Nb-rich regions had Ta contents that were much lower than the surrounding main phase; and 2) the Nb concentration reached a maximum at the center of the features and appeared to decrease radially. In addition, microcracks were observed near Nb-rich regions, which may

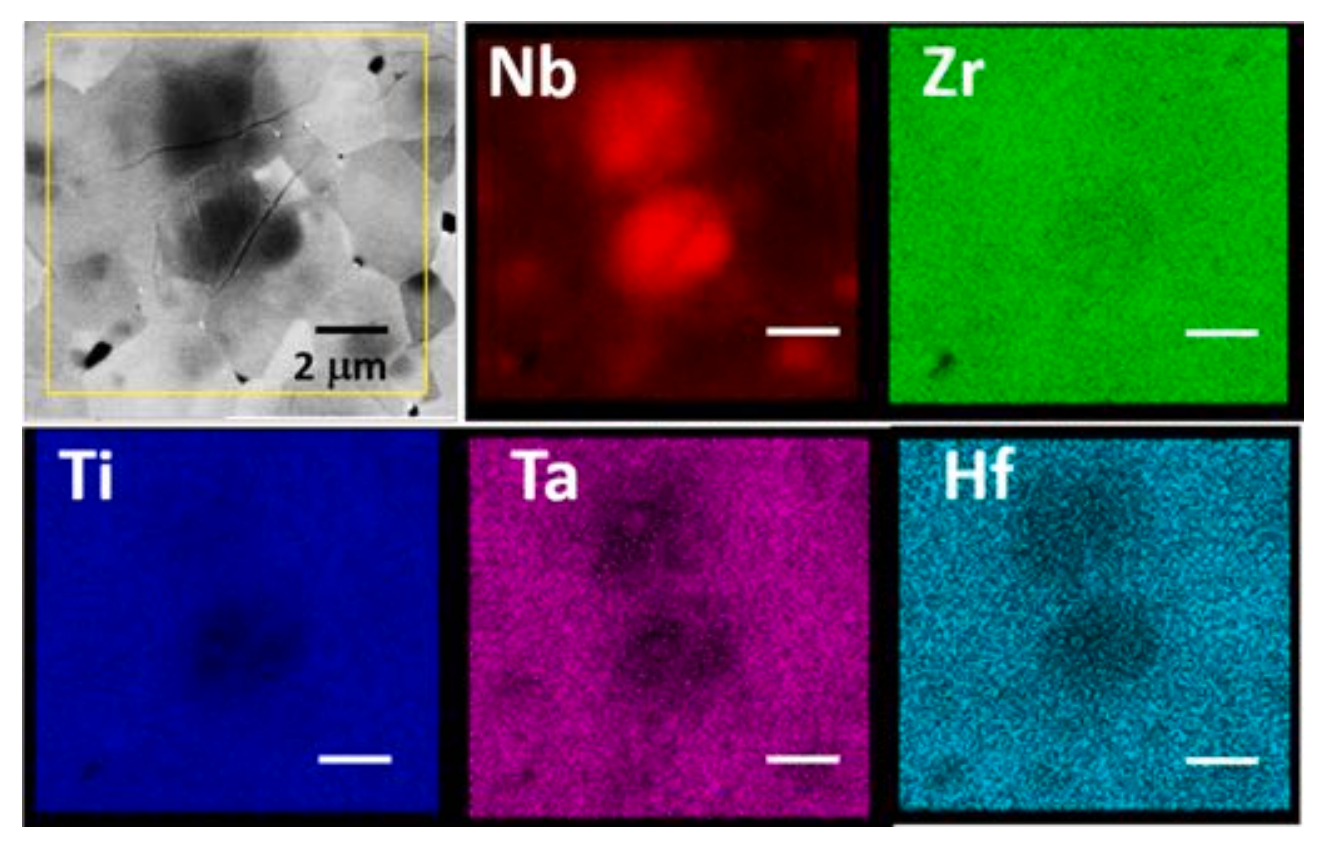


Fig. 7. SEM image for HEB20N and related elemental maps from the yellow box area: a 15 keV energy beam was used for mapping (For interpretation of the references to colour in this figure legend, the reader is referred to the web version of this article).

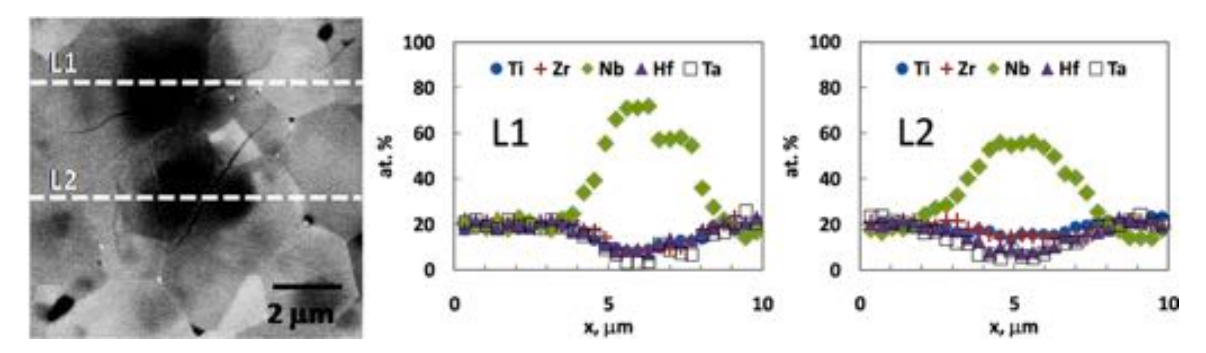


Fig. 8. SEM image for HEB20N and an elemental line scan across line L1 and L2, both 10 microns wide: 15kev energy beam was used. The atomic percentages of the single TMs were normalized to 100 %.

indicate a thermal expansion mismatch between the Nb-rich and the main HEB phase. The mechanism of microcrack formation will be the subject of a future study.

Previous studies reported that $(Hf_{0.2}, Zr_{0.2}, Ti_{0.2}, Ta_{0.2}, Nb_{0.2})B_2$ ceramics were composed of a single HEB phase, although Nb-rich regions were observed in the EDS maps [4,6,15–17]. Nb segregation was not detected by XRD in previous studies, because the two HEB phases have similar lattice parameters, which resulted in overlapped peaks at angles in the XRD patterns below 90° 2-theta. However, in the present study, Nb segregation was observed by changing the Nb contents and then carefully analyzing the results from XRD and SEM-EDS. Reasons for the Nb segregation could be low solubility of NbB₂ in other transition metal borides, slow diffusion of Nb during synthesis/densification, or phase separation at some point in the densification cycle. The mechanism of Nb segregation will be the subject of future studies.

3.5. Mechanical properties

Some measured properties of the HEB ceramics with different Nb contents are summarized in Table 3. Young's modulus was 534 ± 7 GPa for HEB0N, but increased to 555 ± 8 GPa for HEB5N, and 544 ± 8 GPa for HEB20N. The addition of Nb increased the Young's modulus of HEB ceramics. However, Young's modulus decreased as Nb content increased from 5 at% to 20 at%, presumably due to the increase in residual porosity, the effect of the larger amount of the Nb-rich phase, and, possibly, the presence of microcracking near Nb-rich regions caused by the increase in amount of the second HEB phase. Shear modulus also decreased slightly as Nb content increased, from 235 ± 3 GPa for HEB0N to 221 ± 3 GPa for HEB20N. Higher Young's modulus values for (Hf_{0.2}, Zr_{0.2}, Ti_{0.2}, Ta_{0.2}, Nb_{0.2})B₂ ceramics were obtained in the present study compared to the value of 500 GPa reported in a previous study due to higher relative density achieved in the present study.

Fig. 9 shows Vickers hardness as a function of Nb content. Hardness

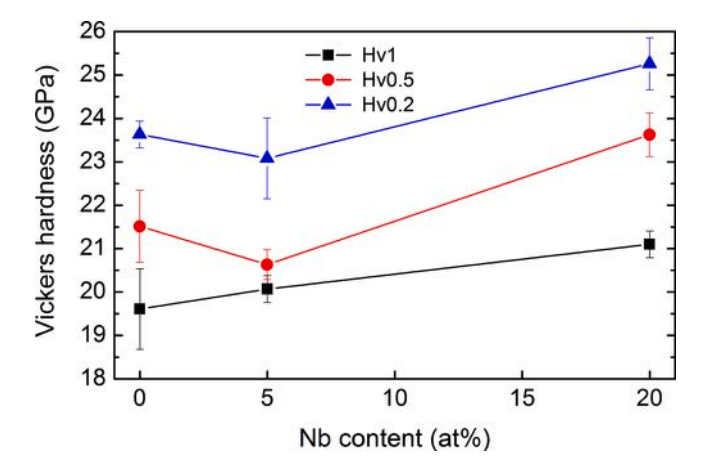


Fig. 9. Vickers hardness of HEB0N, HEB5N and HEB20N as a function of Nb content.

measured under a load of 9.8 N increased from 19.6 \pm 0.9 GPa for HEB0N to 21.1 \pm 0.3 GPa for HEB20N. The increase in hardness with increasing Nb content could be due to the decrease in grain size associated with the presence of the second phase. In contrast, hardness measured under loads of 4.9 N and 2.0 N decreased as Nb content increased from 0 to 5 at% because the indentation sizes were smaller than grain size of HEBON, and larger than grain size of HEB5N. However, hardness measured under loads of 4.9 N and 2.0 N increased as Nb content increased from 5 at% to 20 at%. The increase in Nb content resulted in an increase in the amount of the Nb-rich second phase, which refined grain size of the main HEB phase, which improved the hardness [26,29]. The hardness value of 25.3 \pm 0.6 GPa measured for (Hf_{0.2},Zr_{0.2}, Ti_{0.2},Ta_{0.2},Nb_{0.2})B₂ ceramics at a load of 2.0 N in the present study was comparable to the value of 25.6 \pm 0.8 GPa from one study [12], but higher than the values ranging from 17.5 GPa to 22.7 GPa [4,6,16] for ceramics that contained either residual porosity or oxide impurities.

4. Conclusions

Dense high-entropy (Hf,Zr,Ti,Ta,Nb)B $_2$ ceramics with Nb contents ranging from 0 to 20 at% were produced at 2100 °C by two-step spark plasma sintering of powder mixtures synthesized by boro/carbothermal reduction. The addition of Nb reduced the particle size of the assynthesized powder mixtures from 0.6 μ m to 0.3 μ m. XRD results indicated that a single-phase with hexagonal structure was detected in composition without Nb, while two overlapping high-entropy boride (HEB) phases with hexagonal structure were present in compositions with Nb. SEM-EDS analysis indicated that the secondary HEB phases were a Nb-rich HEB phase formed by Nb segregation. The addition of Nb resulted in the presence of Nb-rich secondary HEB phases which increased as Nb content increased to 20 at% as shown in SEM-EDS maps or focused line scans.

The relative density of HEB ceramics decreased from 100 % to 99.5 % as Nb content increased from 0 to 20 at%. The average grain size decreased from 13.9 \pm 5.5 μm for composition without Nb to 5.6 \pm 2.1 μm and 5.2 \pm 2.0 μm for compositions containing 5 at% and 20 at% Nb, respectively. The decrease in grain size with increasing Nb content was due to the suppression of grain growth by the Nb-rich secondary HEB phase. The addition of Nb resulted in a slight increase in Young's modulus and a slight decrease in shear modulus. Young's modulus was 534 \pm 7 GPa for HEB0N, which increased to 555 \pm 8 GPa for HEB5N, and 544 \pm 8 GPa for HEB20N. Shear modulus decreased from 235 \pm 3 GPa for HEB0N to 221 \pm 3 GPa for HEB20 N. Hardness measured under a load of 9.8 N increased from 19.6 \pm 0.9 GPa for HEB0N to 21.1 \pm 0.3 GPa for HEB20N. The increase in Vickers hardness was due to the reduction of grain size by the presence of Nb-rich secondary phase by Nb

segregation and the increase in the amount of Nb-rich secondary phase.

Declaration of Competing Interest

The authors report no declarations of interest.

Acknowledgements

This research was conducted as part of the Enabling Materials for Extreme Environments Signature Area at Missouri S&T. Support for the project was also provided by the National Science Foundation through grant CMMI-1902069. The authors thank Dr. Eric Bohannan for XRD data refinement, and Dr. Wei-Ting Chen and Dr. Clarissa A. Wisner for SEM analysis in the Advanced Materials Characterization Laboratory.

References

- E.J. Wuchina, E. Opila, M.M. Opeka, W.G. Fahrenholtz, I.G. Talmy, UHTCs: ultrahigh temperature ceramic materials for extreme environment applications, Electrochem. Soc. Interface 16 (2007) 30–36.
- [2] J.W. Zimmermann, G.E. Hilmas, W.G. Fahrenholtz, R.B. Dinwiddie, W.D. Porter, H. Wang, Thermophysical properties of ZrB2 and ZrB₂-SiC ceramics, J. Am. Ceram. Soc. 91 (2008) 1405–1411, https://doi.org/10.1111/j.1551-2916.2008.02268.x.
- [3] W.G. Fahrenholtz, G.E. Hilmas, I.G. Talmy, J.A. Zaykoski, Refractory diborides of zirconium and hafnium, J. Am. Ceram. Soc. 90 (2007) 1347–1364, https://doi.org/ 10.1111/j.1551-2916.2007.01583.x.
- [4] J. Gild, Y.Y. Zhang, T.J. Harrington, S.C. Jiang, T. Hu, M.C. Quinn, W.M. Mellor, N. X. Zhou, K.H. Vecchio, J. Luo, High-entropy metal diborides: a new class of high entropy materials and a new type of ultrahigh temperature ceramics, Sci. Rep. 6 (2016) 37946, https://doi.org/10.1038/srep37946.
- [5] L. Feng, W.G. Fahrenholtz, G.E. Hilmas, Processing of dense high-entropy boride ceramics, J. Eur. Ceram. Soc. 40 (2020) 3815–3823, https://doi.org/10.1016/j. jeurceramsoc.2020.03.065.
- [6] F. Monteverede, F. Saraga, M. Gaboardi, Compositional disorder and sintering of entropy stabilized (Hf,Nb,Ta,Ti,Zr)B₂ solid solution powders, J. Eur. Ceram. Soc. 40 (2020) 3807–3814, https://doi.org/10.1016/j.jeurceramsoc.2020.04.026.
- [7] W.G. Fahrenholtz, G.E. Hilmas, Ultra-high temperature ceramics: materials for extreme environments, Scr. Mater. 129 (2017) 94–99, https://doi.org/10.1016/j. scriptamat.2016.10.018.
- [8] A.S. Brown, Hypersonic designs with a sharp edge. Aerospace America, 1997.
- [9] L. Feng, W.G. Fahrenholtz, G.E. Hilmas, Two-step synthesis process for highentropy diboride powders, J. Am. Ceram. Soc. 103 (2020) 724–730, https://doi. org/10.1111/jace.16801.
- [10] F. Monteverede, F. Saraga, Entropy stabilized single-phase (Hf,Nb,Ta,Ti,Zr)B₂ solid solution powders obtained via carbo/boro-thermal reduction, J. Ally. Compds. 824 (2020) 153930, https://doi.org/10.1016/j.jallcom.2020.153930.
- [11] D. Liu, T.Q. Wen, B.L. Ye, Y.H. Chu, Synthesis of superfine high-entropy metal diboride powders, Scr. Mater. 167 (2019) 110–114, https://doi.org/10.1016/j. scriptamat.2019.03.038.
- [12] J.F. Gu, J. Zou, S.K. Sun, H. Wang, S.Y. Yu, J.Y. Zhang, W.M. Wang, Z.Y. Fu, Dense and pure high-entropy metal diboride ceramics sintered from self-synthesized powders via boro/carbothermal reduction approach, Sci. China Mater. 62 (2019) 1898–1909, https://doi.org/10.1007/s40843-019-9469-4.
- [13] G. Tallarita, R. Licheri, S. Garroni, R. Orru, G. Cao, Novel processing route for the fabrication of bulk high-entropy metal diborides, Scr. Mater. 158 (2019) 100–104, https://doi.org/10.1016/j.scriptamat.2018.08.039.
- [14] G. Tallarita, R. Licheri, S. Garroni, S. Barbarossa, R. Orru, G. Cao, High-entropy transition metal diborides by reactive and non-reactive spark plasma sintering: a comparative investigation, J. Eur. Ceram. Soc. 40 (2020) 942–952, https://doi. org/10.1016/j.jeurceramsoc.2019.10.031.
- [15] Y. Zhang, W.M. Guo, Z.B. Jiang, Q.Q. Zhu, S.K. Sun, Y. You, K. Plucknett, H.T. Lin, Dense high-entropy boride ceramics with ultra-high hardness, Scr. Mater. 164 (2019) 135–139, https://doi.org/10.1016/j.scriptamat.2019.01.021.
- [16] Y. Zhang, Z.B. Jiang, S.K. Sun, W.M. Guo, Q.S. Chen, J.X. Qiu, K. Plucknett, H. T. Lin, Microstructure and mechanical properties of high-entropy borides derived from boro/carbothermal reduction, J. Eur. Ceram. Soc. 39 (2019) 3920–3924, https://doi.org/10.1016/j.jeurceramsoc.2019.05.017.
- [17] Y. Zhang, S.K. Sun, W. Zhang, Y. You, W.M. Guo, Z.W. Chen, J.H. Yuan, H.T. Lin, Improved densification and hardness of high-entropy diboride ceramics from fine powders synthesized via borothermal reduction process, Ceram. Int. 46 (2020) 14299–14303. https://doi.org/10.1016/j.ceramint.2020.02.214.
- [18] S. Otani, T. Aizawa, N. Kieda, Solid solution ranges of zirconium diboride with other refractory diborides: HfB₂, TiB₂, TaB₂, NbB₂, VB₂ and CrB₂, J. Ally. Compds. 475 (2009) 273–275, https://doi.org/10.1016/j.jallcom.2008.08.023.
- [19] F. Monteverde, A. Bellosi, S. Guicciardi, Processing and properties of zirconium diboride-based composites, J. Eur. Ceram. Soc. 22 (2002) 279–288, https://doi. org/10.1016/S0955-2219(01)00284-9.
- [20] Y.F. Ye, Q. Wang, J. Lu, C.T. Liu, Y. Yang, High-entropy alloy: challenges and prospects, Mater. Today 19 (2016) 349–362, https://doi.org/10.1016/j. mattod.2015.11.026.

- [21] O.N. Senkov, S.V. Senkova, C. Woodward, D.B. Miracle, Low-density, refractory multi-principal element alloys of the Cr-Nb-Ti-V-Zr system: microstructure and phase analysis, Acta Mater. 61 (2013) 1545–1557, https://doi.org/10.1016/j. actamat.2012.11.032.
- [22] L. Feng, W.G. Fahrenholtz, G.E. Hilmas, Y. Zhou, Synthesis of single-phase high-entropy carbide powders, Scr. Mater. 162 (2019) 90–93, https://doi.org/10.1016/j.scriptamat.2018.10.049.
- [23] G.V. Samsonov, T.I. Serebryakova, V.A. Neronov, Borides, Atomizdat, Moscow, 1975.
- [24] G.V. Samsonov, K.I. Portnoi, Alloys based on high-temperature compounds (splavy na osnove tugoplavkikh soedineniy), Oboronnoi Prom., Moscow, 1961 (English Translation)
- [25] H.L. Wang, S.H. Lee, L. Feng, The processing and properties of (Zr,Hf)B₂-SiC nanostructured composites, J. Eur. Ceram. Soc. 34 (2014) 4105–4109, https://doi.org/10.1016/j.jeurceramsoc.2014.05.020.
- [26] L. Feng, W.G. Fahrenholtz, G.E. Hilmas, Low-temperature sintering of single-phase, high-entropy carbide ceramics, J. Am. Ceram. Soc. 102 (2019) 7217–7224, https://doi.org/10.1111/jace.16672.
- [27] M.A. Kuzenkova, P.S. Kislyi, O.V. Zaverukha, Y.B. Kus'ma, Structure and properties of zirconium diboride-tungsten alloys, Sov. Powder Metall. Met. Ceram. 10 (1971) 879–883
- [28] P.S. Kislyi, M.A. Kuzenkova, Regularities of sintering of zirconium diboride-molybdenum alloys, Sov. Powder Metall. Met. Ceram. 5 (1966) 363–365, https://doi.org/10.1007/BF00775989.
- [29] L. Feng, W.G. Fahrenholtz, G.E. Hilmas, J. Watts, Y. Zhou, Densification, microstructure, and mechanical properties of ZrC-SiC ceramics, J. Am. Ceram. Soc. 102 (2019) 5786–5795, https://doi.org/10.1111/jace.16505.